9 Particle physics with CMS

E. Alagöz, C. Amsler, V. Chiochia, Hp. Meyer, B. Millan Mejias, C. Regenfus, P. Robmann, J. Rochet, T. Rommerskirchen, A. Schmidt, S. Steiner, D. Tsirigkas, and L. Wilke

In collaboration with: Paul Scherrer Institut (PSI) and the CMS Collaboration

The silicon pixel detector is the innermost component of the CMS apparatus (1) at the LHC, with which a precise reconstruction of charged particles and secondary vertices from heavy quark decays will be performed. The barrel pixel detector (48 million pixels) consists of three cylindrical layers at radii of 4.4 cm, 7.4 and 10.2 cm, with a length of 53 cm. Four forward disks (18 million pixels) are located along the beam axis, two on each side (18 million pixels) at $\pm$34 cm and $\pm$47 cm from the collision point.

We were involved in the design, construction and commissioning of the barrel pixel detector. We have provided equipment and have led prototype tests on CERN beams (2; 3; 4), measuring sensor performances such as position resolution, detection efficiency, charge sharing and Lorentz deflection, before and after irradiation. We have also contributed to the development and commissioning of the readout chip (ROC) (5). We have developed and built in the Institute workshop the mechanical and cooling structure and the two service tubes which provide the coolant and power, and transfer the signals to and from the pixel detector (6).

In 2008 we continued the analysis of the test beam data taken in 2006. We had used a telescope with pixel sensors (150 μm $\times$ 100 μm pixels), two in front and two behind the irradiated pixel detector under test. Irradiated sensors were kept at -10°C in a cooling box with Peltier elements. The pixels were bump-bonded to the final CMS pixel readout chips. The apparatus was located in a Helmholtz superconductor 3T magnet and exposed to a 150 GeV π^--beam.

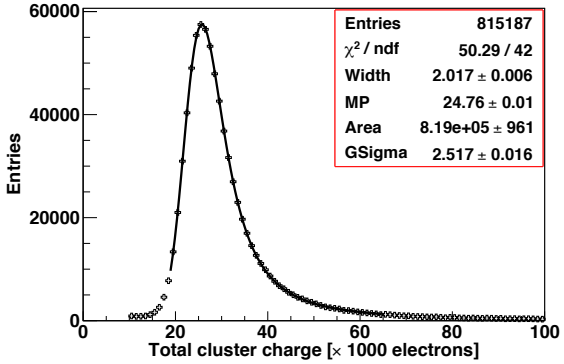

Figure 9.1: Cluster charge distribution for the un-irradiated sensor. The solid line is a Gaussian convoluted Landau fit (from [4]).

The charge distribution of an un-irradiated sensor operated at 150 V bias voltage in a 3T magnetic field is shown in Fig. 9.1. The solid line is the Gaussian convoluted Landau fit. The most probable value for the cluster charge is around 24'760 electrons. For irradiated pixels one observes a charge loss which is partially recovered by applying higher bias voltages. The collected charge is reduced to 77% (38%)

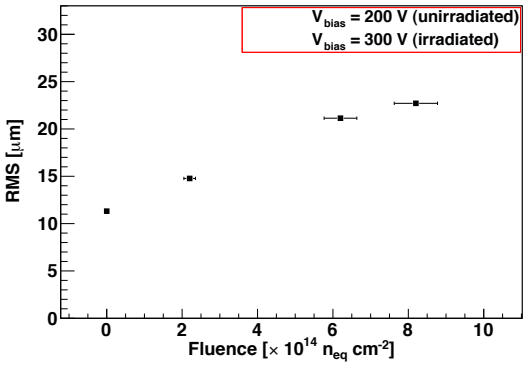

Figure 9.2: Position resolution as a function of irradiation fluence for perpendicular incidence (from [4]).

for a fluence of 2.2×10^{14} (8.2×10^{14}) $\mathrm{n_{eq}cm^{-2}}$. The spatial resolution as a function of irradiation fluence is shown in Fig. 9.2. The degradation in the position resolution is due to charge loss as a result of radiation damage. In addition, the higher bias voltage reduces the Lorentz angle, leading to reduced charge sharing among adjacent pixels.

We have developed reconstruction and physics analysis software, in particular track and vertex reconstruction (7; 8), and constraining kinematic fits (9). This activity continues with the development of b-tagging algorithms (10). We plan to exploit the first data from LHC for a study of $B_s \rightarrow J/\psi\ \phi$ (11; 12) and for a measurement of the $t\bar{t}$-cross section (13). More information and related publications can be found in previous annual reports.

We are also preparing a search for supersymmetry in dijet events (14). The study is focused on the SUSY parameter space where squarks are pair-produced and both decay into a quark and a neutralino. The latter escapes undetected and gives rise to missing energy. Although the background from QCD dijet events is overwhelming, powerful discriminating variables can be found due to the particular kinematics of SUSY events. This should enable results already with early collision data.

CMS (and the other LHC experiments) will produce enormous amounts of data to be processed and analyzed. This will be achieved by tiered computing architectures, dividing the data streams and processing tasks among several computing centers. The Tier-0 center is located directly at the experiment. A small number of Tier-1 centers perform the first steps of re-processing. The skimmed data are accessible from Tier-2 centers (CSCS at Manno for us) and Tier-3 centers (PSI for us). The final stage of analysis is usually performed locally with small Tier-4 clusters, managed by the research groups themselves.

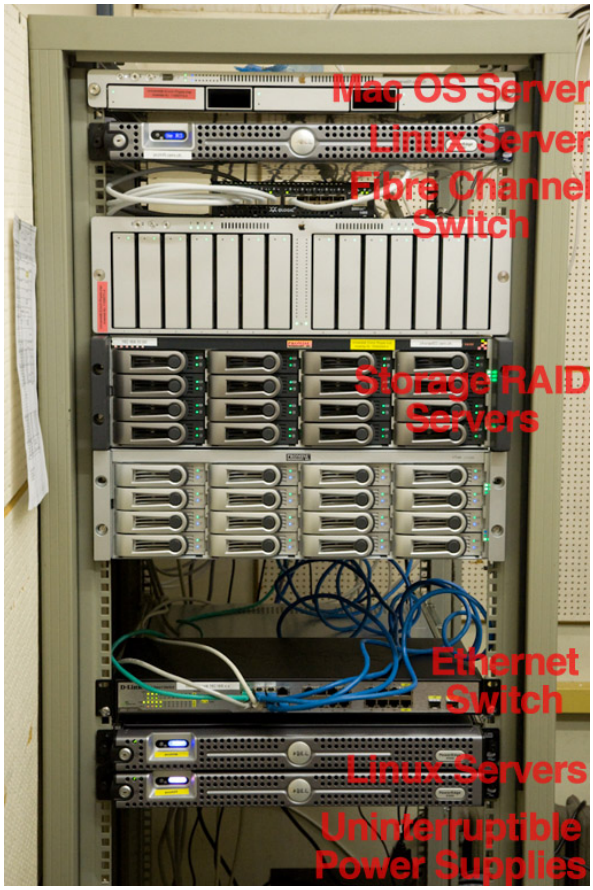

Figure 9.3: One of the two racks of the UZH computing cluster. Visible are the 35 TeraByte storage RAID servers and three of the Linux servers, as well as some switching and cabling infrastructure.

During 2008 we purchased and installed our own computing cluster at CERN. It consists of 28 CPU cores running at 3 GHz and 35 TeraByte of redundant (RAID) storage space, connected via a high-speed Fiber Channel Network. Efficient and easy access to all CERN services is available, since the whole cluster is located inside of the CERN network. Figure 9.3 shows a photograph of one of the two racks of the cluster. The computing nodes are running the Scientific Linux (SLC4) average operating system, and the data storage is mounted on each computing node via the network file system (NFS). An air conditioning system was installed to provide the necessary cooling power to keep the room temperature

well below 30 degrees. Uninterruptible power supplies prevent potential damage caused by the frequent power glitches and outages at CERN. Our computing cluster was already used for the cosmic runs in 2008.

We are responsible for the implementation, maintenance and validation of the barrel pixel geometry in the Monte-Carlo simulation. The description in the simulation (6) needs to be as precise as possible to reproduce the exact amount of material interactions. Such interactions deteriorate the trajectories of particles and influence the measurements in the outer detectors (strip tracker, calorimeters and muon detectors). Figure 9.4 shows for example the material thickness in the CMS tracker as a function of pseudorapidity which reveals the relatively large thickness in the regions of pseudorapidity $1 < \eta < 1.5$. The weight of the pixel detector implemented in the Monte-Carlo simulation has been compared with its real weight and the agreement was found to be within 6%.

The innermost layer of the pixel detector provides information on secondary vertices and impact parameters for b- and τ-decays which are relevant to Higgs searches. Studies of impact parameter resolution, track seeding, b- and τ-tagging efficiency will be performed. Before physics research can start, tasks such as software detector alignment and calibration need to be performed during the early phase of detector operation. Detector alignment, crucial for vertex reconstruction and b-tagging, is expected to improve with time and luminosity.

We have simulated the expected efficiency of identifying b-jets ("b-tagging efficiency") for various degrees of detector alignment (Fig. 9.5). At startup only information from survey measurements and cosmic muon tracks can be used to perform the detector alignment. At 10 pb^{-1} the tracker can be aligned by using hadrons and muons from the decays of low mass resonances such as J/ψ and Υ. At 100 pb^{-1} high p_T muons from Z- and W-boson decays become available, at which time the misalignment of the pixel tracker is expected to be around 20μm. The tracker is finally aligned with an integrated luminosity of 1 fb^{-1} which can be achieved within one year of detector operation.

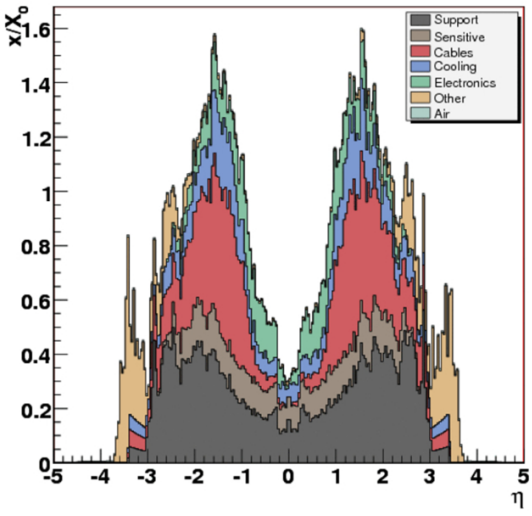

Figure 9.4:
Material thickness X (in radiation lengths X_0) in the CMS tracker, as a function of pseudorapidity η.

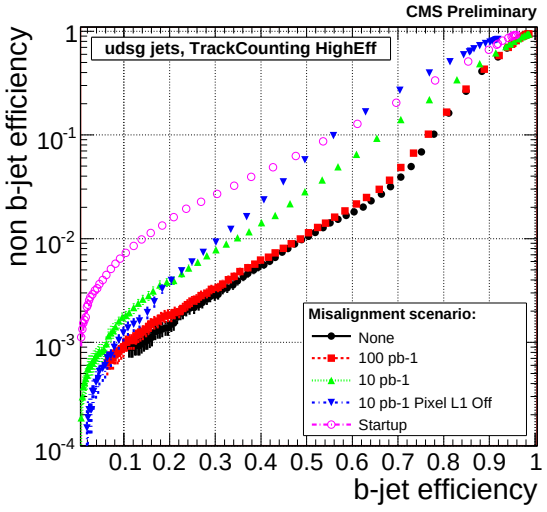

Figure 9.5: Expected misidentification efficiency versus b-jet tagging efficiency for different values of integrated luminosity with corresponding improvements in detector alignment.

The Monte-Carlo simulation then needs to be tuned according to detector performance. Large amounts of events need to be simulated using our Tier-3 facility at PSI. The simulation is time consuming (up to two minutes on a modern CPU and hundreds of millions of events are needed). A fast Monte-Carlo simulation is provided which uses parametrizations based on the full simulation and a simplified detector geometry (10; 15). The fast simulation is 100 – 1000 $\times$ faster than the full simulation.

The construction and installation of the pixel detector was completed in 2008 and operation started with beam on 10 September. Following the incident on 19 September, the detector was commissioned with cosmic ray data. Some 300 million events were collected until the end of the year. Data was taken without magnetic field ("CRUZET" data) and with 3.8 T ("CRAFT " data). With magnetic field turned on about 80'000 events had a muon crossing the pixel detector. Figure 9.6 shows one of the cosmic ray events. The various CMS subdetectors could be aligned with these data and the detection efficiencies measured. In particular, 99% (96%) of the barrel (forward) pixels was found to be operational.

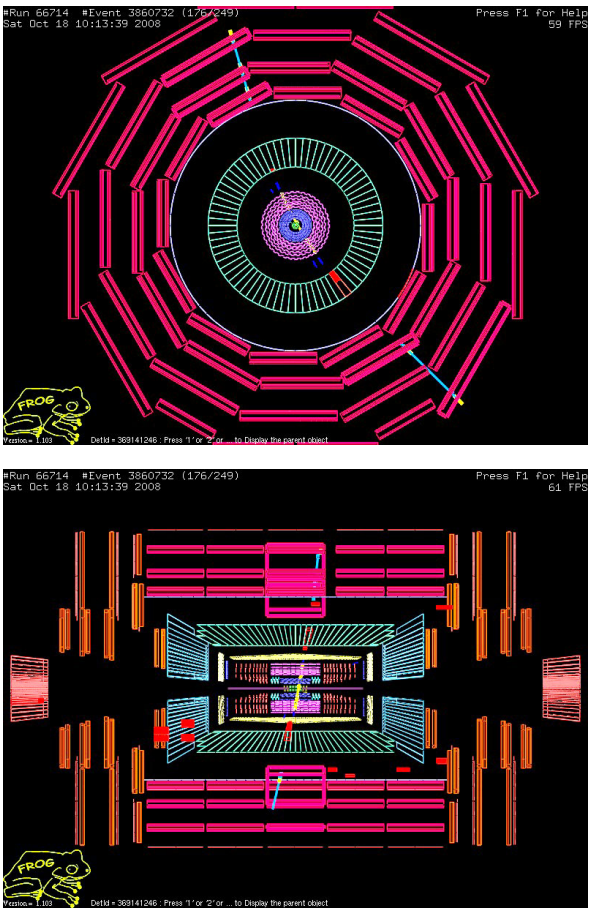

Figure 9.6: A spectacular event display showing a cosmic muon crossing CMS and the pixel detector.

The tracking performance of the CMS detector depends crucially on the alignment of the tracking devices, in particular of the pixel detector. Different alignment techniques are being used. In one method we use cosmic ray tracks traversing the pixel detector. For the pattern recognition this leads to two tracks emerging from the detector center. In a first step we use the outer strips from the tracker to determine the trajectories and to compute the difference (residuals) between the predicted and measured hits in the pixel detector. This is done for every sensor module. The average residual is then determined and used to align the detector.

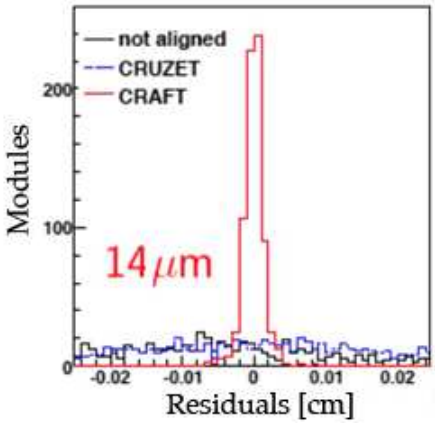

Figure 9.7: Average residuals for the barrel pixels before and after alignment with cosmic rays with field off (blue) and field on (red).

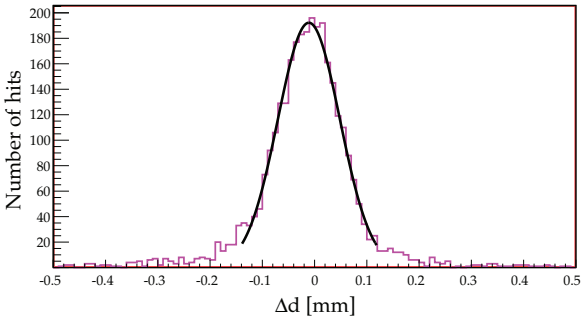

Figure 9.8: Distribution of the difference Δd between the distances to the detector axis for the two half tracks originating from a high momentum cosmic muon.

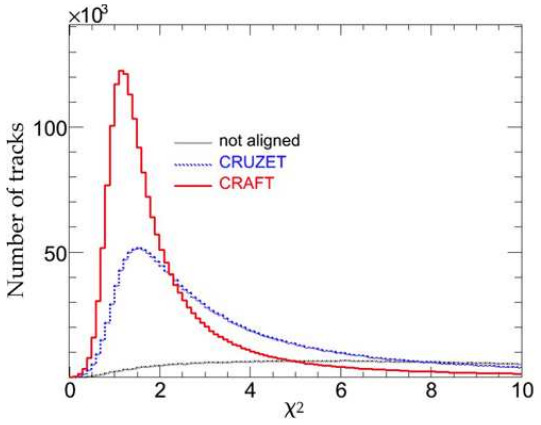

Figure 9.9: χ^2-distribution for reconstructed cosmic ray tracks, before and after alignment without magnetic field (CRUZET) and with magnetic field (CRAFT).

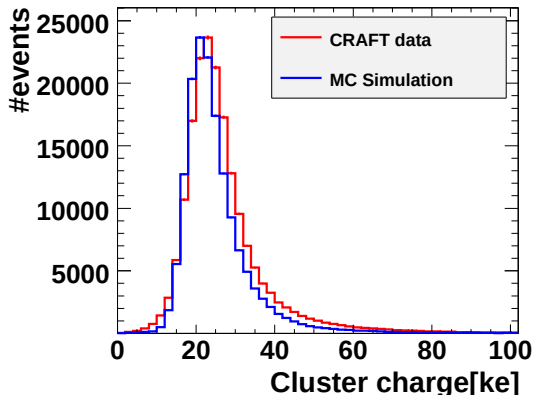

Figure 9.10: Distribution of the cluster charge measured in the barrel pixel detector.

Figure 9.7 shows the distribution of the average residuals for the barrel pixels before and after alignment. The accuracy on the alignment is around 14 μm r.m.s. Figure 9.8 shows the difference of distances to the detector axis after detector alignment with cosmic rays of more than 20 GeV/c transverse momentum, which is a measure for the impact parameter resolution. The r.m.s resolution on the impact parameter is 59 $\pm$ 1 μm. Figure 9.9 shows the spectacular improvement on the track reconstruction that could already be achieved with cosmics (described below). However, since cosmic rays are mostly vertical, the alignment of detectors lying in the horizontal plane will have to be performed with collision data.

Studying the differences between simulation and data helped to improve our understanding of the pixel detector. One of the most important variables is the cluster charge. Several effects have been identified which are not be reproduced in Monte-Carlo simulations, such as the dependence of the readout time on the signal amplitude. These effects have been studied extensively. Figure 9.10 shows the cluster charge distribution after selection cuts, as measured with field on (CRAFT) in the barrel pixel detector. The simulation reproduces already quite well the peak-position and the measured width.

In the 3.8 T field of CMS the electrons produced by a charged particle passing through the pixel detector drift perpendicularly to the magnetic field in the sensor (Fig. 9.11). This leads to a non-vanishing

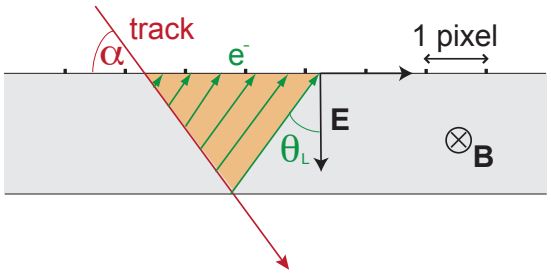

Figure 9.11: Lorentz angle θ_L (from [11]).

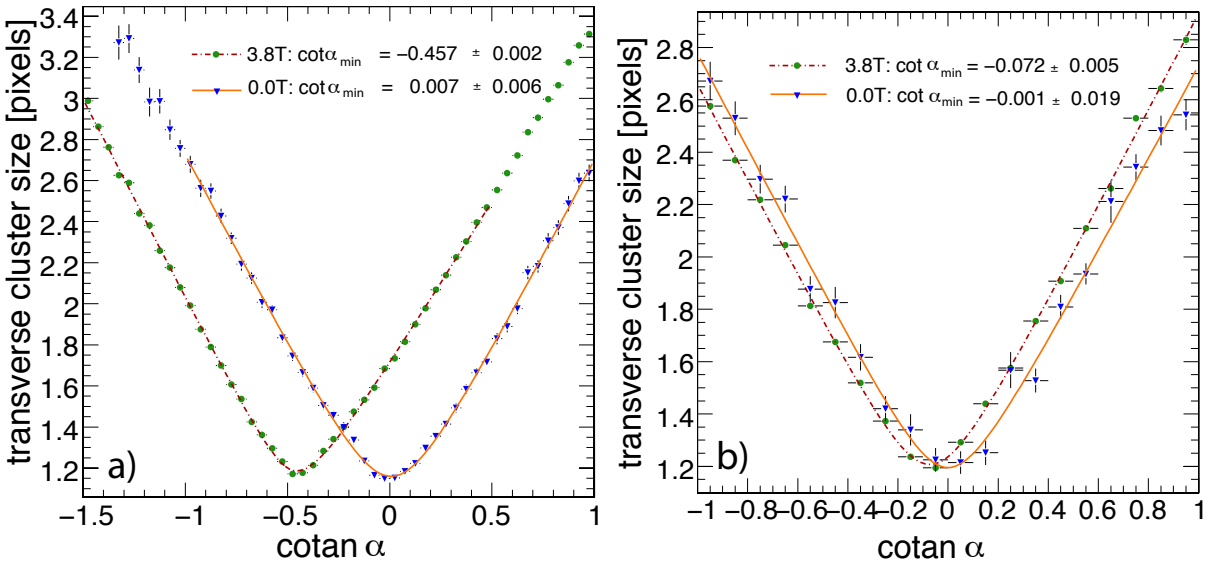

Figure 9.12: Measured cluster size as a function of incidence angle α for un-irradiated pixels. The predictions (lines) are compared to data at 3.8 T (circles) and 0 T (triangles) for the barrel (a) and forward (b) pixel detector. Only statistical errors are shown (from [11]).

Lorentz angle θ_L and hence a shift of the hit coordinate. The correction (up to 120 μm) will decrease as a function of time. This is due to the increasing bias voltage needed to compensate for radiation damage (see below). Furthermore, since the irradiation is not uniform across the detector, each module will evolve differently. The Lorentz angle will therefore be estimated directly from data. With collision data this is done by comparing the observed shapes of charged clusters with the reconstructed tracks in the tracker (16).

Meanwhile we have determined θ_L from cosmic rays. The spread of the charge distribution over neighboring pixels depends on the particle incidence angle α and is minimum when the particle flies along the drift direction (when α = 90° + θ_L, see Figs. 9.11 and 9.12). Hence θ_L is measured by finding the minimum of the mean cluster size distribution, measured as a function of track incidence angle. The barrel pixel detector modules are perpendicular to the magnetic field while the forward modules are inclined by α = 20° relative to the magnetic field, leading to in a much lower value θ_L for the forward detector. The results (Fig. 9.12) are then compared to the PIXELAV simulation (17) of the pixel detector. The measured values agree well with the predicted values (see also Table 9.1). Cosmic data without magnetic field (for which θ_L = 0) are used as a consistency check.

Table 9.1: Measured values for $\tan\theta_L$ at 3.8 T for un-irradiated pixels, compared with expectations for the barrel and forward pixel detectors.

	$\tan\theta_L$	
	measurement	PIXELAV prediction
barrel	$-0.457(2)$	$-0.452(2)$
forward	$-0.072(5)$	$-0.080(5)$

Operation with cosmic rays will resume in summer 2009 while first collisions with 10 TeV protons are expected in autumn.

[1] S. Chatrchyan *et al.* (CMS Collaboration), Journal of Instrumentation **3** (2008) S08004.

[2] Y. Allkofer *et al.*, Nucl. Instr. Meth. in Phys. Research **A 584** (2008) 25.

[3] V. Chiochia *et al.*, Nucl. Instr. Meth. in Phys. Research **A 568** (2006) 51; V. Chiochia *et al.*, IEEE Trans. Nucl. Sci. **52** (2005) 1067.

[4] E. Alagöz, PhD Thesis (in preparation).

[5] C. Hörmann, PhD Thesis, Universität Zürich (2006).

[6] C. Amsler *et al.*, submitted to Journal of Instrumentation.

[7] R. Frühwirth and T. Speer, Nucl. Instr. and Meth. in Phys. Res. **A 534** (2004) 217.

[8] R. Frühwirth, K. Prokofiev, T. Speer, P. Vanlaer and W. Waltenberger, Nucl. Instr. Meth. in Phys. Res. **A 502** (2003) 699.

[9] K. Prokofiev, PhD Thesis, Universität Zürich (2005).

[10] A. Schmidt, Nucl. Phys. B - Proceedings Supplements **187** (2009) 216.

[11] L. Wilke, PhD Thesis (in preparation).

[12] B. Millan Mejias, PhD Thesis (in preparation).

[13] D. Tsirigkas, PhD Thesis (in preparation).

[14] T. Rommerskirchen, PhD Thesis (in preparation), CMS Note PAS SUS-08-005.

[15] A. Schmidt, 2008 IEEE Nuclear Science Symposium Conference Record (2008) 2795.

[16] L. Wilke, V. Chiochia, T. Speer, CMS Note 2008/012.

[17] M. Swartz, Nucl. Instrum. Meth. **A 511** (2003) 88.